Fluorescent metallacycle-cored polymers via covalent linkage and their use as contrast agents for cell imaging

Mingming Zhang[a,1], Shuya Li[b], Xuzhou Yan[a], Zhixuan Zhou[a], Manik Lal Saha[a], Yu-Cai Wang[b,1], and Peter J. Stang[a,1]

[a]Department of Chemistry, University of Utah, Salt Lake City, UT 84112; and [b]The Chinese Academy of Sciences Key Laboratory of Innate Immunity and Chronic Diseases, School of Life Sciences and Medical Center, University of Science & Technology of China, Hefei 230027, People's Republic of China

Contributed by Peter J. Stang, August 3, 2016 (sent for review June 16, 2016; reviewed by Francois N. Diederich, Mostafa El-Sayed, and Jean M. J. Fréchet)

The covalent linkage of supramolecular monomers provides a powerful strategy for constructing dynamic polymeric materials whose properties can be readily tuned either by the selection of monomers or the choice of functional linkers. In this strategy, the stabilities of the supramolecular monomers and the reactions used to link the monomers are crucial because such monomers are normally dynamic and can disassemble during the linking process, leading to mixture of products. Therefore, although noncovalent interactions have been widely introduced into metallacycle structures to prepare metallosupramolecular polymers, metallacycle-cored polymers linked by covalent bonds have been rarely reported. Herein, we used the mild, highly efficient amidation reaction between alkylamine and *N*-hydroxysuccinimide-activated carboxylic acid to link the pendent amino functional groups of a rhomboidal metallacycle 10 to give metallacycle-cored polymers P1 and P2, which further yielded nanoparticles at low concentration and transformed into network structures as the concentration increased. Moreover, these polymers exhibited enhanced emission and showed better quantum yields than metallacycle 10 in methanol and methanol/water (1/9, vol/vol) due to the aggregation-induced emission properties of a tetraphenylethene-based pyridyl donor, which serves as a precursor for metallacycle 10. The fluorescence properties of these polymers were further used in cell imaging, and they showed a significant enrichment in lung cells after i.v. injection. Considering the anticancer activity of rhomboidal Pt(II) metallacycles, this type of fluorescent metallacycle-cored polymers can have potential applications toward lung cancer treatment.

fluorescent polymers | supramolecular coordination complex | covalent linkage | aggregation-induced emission | cell imaging

Fluorescent polymers have received much attention in the chemical and life sciences due to their promising applications in biological labeling, tracking, monitoring, imaging, and diagnostics (1–3). Compared with other fluorophores such as small molecules and quantum dots, they are advantageous as biomaterials because of their good biocompatibility, ease of preparation, and biomimetic character (4–6). Conventional fluorophores show good emission in dilute solution but experience varying degrees of aggregation-caused quenching due to the intense intermolecular interactions, which will decay or relax the excited state back to the ground state via nonradiative channels (7). Such fluorophores are not ideal candidates for the preparation of fluorescent polymers, because they need to be aggregated by the polymerization process, which will more or less decrease the fluorescence emissions and the quantum yields of the derived fluorescent polymers.

In 2001, Tang and coworkers (8) reported an opposite fluorescence effect named as aggregation-induced emission (AIE). In such cases, fluorophores are nearly nonemissive as discrete molecules, but they exhibit strong fluorescence in concentrated solution or in the solid state due to the restriction of molecular rotations, which will decrease the nonradiative decay (7–11). If fluorophores with such AIE properties were used as luminescent sources, the aggregation induced by the polymerization should promote the emission of such polymers.

Coordination-driven self-assembly is an efficient approach to construct supramolecular coordination complexes (SCCs) (12–24). Due to the directionality of metal–ligand bonds and their moderate bond energies, the structures of SCCs can be finely tuned. So far, various SCCs with different geometries, such as 2D metallacycles (25–28) and 3D metallacages (29–32), were successfully prepared by the self-assembly of carefully selected metal acceptors and organic donors. Moreover, metal–ligand interactions show good tolerance of other noncovalent interactions such as hydrogen bonding and host–guest interactions, which were used to construct highly advanced functional supramolecular entities, such as mechanically interlocked molecules (33–35) and supramolecular polymers (36–38), via orthogonal self-assembly.

Although some progress has been made on the functionalization of metallacycles to construct stimuli-responsive supramolecular complexes and polymers (33–38), the covalent linkage (39–41) of metallacycles to synthesize functional polymers has rarely been reported. The main difficulty of this strategy lies in how to maintain the dynamic metallacycle structures during the linking process. To accomplish covalently linked metallacycle-cored polymers, there are several issues to be addressed: (*i*) The metallacycles should be both simple and stable to reduce the possibility of deconstruction;

Significance

Fluorescent polymers play an important role in bioimaging due to their improved brightness, inertness to microenvironment, and good biocompatibility. In this article, we used tetraphenylene (TPE) derivatives that give strong fluorescence emission in an aggregated state as fluorophores and synthesized fluorescent polymers via the covalent linkage of TPE-based rhomboidal Pt(II) metallacycles. Due to the integration of covalent linkage-induced aggregation of the monomers, the aggregation-induced emission character of TPE derivatives together with Pt(II)-based metal–ligand interactions, these polymers exhibit enhanced emission compared with their corresponding precursors, making them applicable as excellent cell imaging agents. Considering the potential anticancer activity of rhomboidal Pt(II) metallacycles, these polymers may serve as theranostic agents for both bioimaging and cancer therapy.

Author contributions: M.Z., Y.-C.W., and P.J.S. designed research; M.Z., S.L., X.Y., Z.Z., and M.L.S. performed research; M.Z. and X.Y. contributed new reagents/analytic tools; M.Z., M.L.S., Y.-C.W., and P.J.S. analyzed data; and M.Z., M.L.S., Y.-C.W., and P.J.S. wrote the paper.

Reviewers: F.N.D., ETH Zurich; M.E.-S., Georgia Institute of Technology; and J.M.J.F., King Abdullah University of Science and Technology.

The authors declare no conflict of interest.

[1]To whom correspondence may be addressed. Email: stang@chem.utah.edu, mingming.zhang@utah.edu, or yucaiwang@ustc.edu.cn.

This article contains supporting information online at www.pnas.org/lookup/suppl/doi:10.1073/pnas.1612898113/-/DCSupplemental.

www.pnas.org/cgi/doi/10.1073/pnas.1612898113

(*ii*) the introduced functional groups should not interfere with the metal–ligand bonds; (*iii*) the reaction used to link the metallacycles should be mild and highly efficient; and (*iv*) any reagents used to promote the reaction should be easy to remove. Herein, by examining the structures of a number of metallacycles and chemical reactions, we chose rhomboidal Pt(II) metallacycles and the amidation reaction to overcome the above-mentioned challenges. Thus, polymers **1** and **2** (**P1** and **P2**) were synthesized by linking a tetraamino-functionalized rhomboidal Pt(II) metallacycle **10** using *N*-hydroxysuccinimide-activated carboxylic acid-based linkers **11** or **12**. Both **P1** and **P2** consist of a tetraphenylethene (TPE) derivative which is a well-known AIE fluorophore (7–11). The aggregation of the monomers by polymerization inhibits the rotations of the aromatic rings of TPE, making **P1** and **P2** more emissive than their metallacycle precursor **10**. At higher concentrations, the resulting polymers further aggregate into network structures, thereby even further enhancing their fluorescence, and hence may serve as potentially useful cell imaging agents. By investigating the distribution of **P2** in mice 6 h after i.v. injection, we found that **P2** showed significant enrichment in the lung. Based on the potential anticancer activity of rhomboidal Pt(II) metallacycles (42), these metallacycle-cored polymers may show potential applications as theranostic agents for both cell imaging and tumor therapy.

Results and Discussion

The synthetic procedures for **P1** and **P2** are shown in Fig. 1. A TPE-derivative **8**, having two pyridyl groups for metal coordination and two amino groups for polymerization, was synthesized in a four-step pathway starting from commercially available benzophenone derivatives. The key intermediate TPE-derivative **4** was prepared by a classical McMurry coupling reaction and isolated in 45% yield. After nucleophilic substitution at the phenolic hydroxyl site of **4**, a palladium-catalyzed Suzuki coupling reaction was carried out to obtain the 120° dipyridyl ligand **7**, which was further reduced in the presence of hydrazine to yield ligand **8**. The rhomboidal Pt(II) metallacycle **10** was prepared in quantitative yield by heating the 120° dipyridyl donor **8** and 60° platinum acceptor **9** at 50 °C in methanol for 24 h. Simple stirring of a mixture of **10** with **11** or **12** (1:2 molar ratio) in methanol solution at room temperature for a day, followed by dialysis with methanol, gave **P1** and **P2** in 83% and 86% yields, respectively.

The formation of metallacycle **10** was confirmed by multinuclear NMR (^{31}P and ^{1}H) analysis and electrospray ionization time-of-flight mass spectrometry (ESI-TOF-MS). The $^{31}P\{^{1}H\}$ NMR spectrum of **10** exhibits a sharp singlet (13.92 ppm) with concomitant ^{195}Pt satellites corresponding to a single phosphorous environment (Fig. 2*G*), indicating the formation of a discrete, highly symmetric metallacycle. In the ^{1}H NMR spectrum of metallacycle **10**, the expected downfield chemical shifts were observed for the α-pyridyl protons H_a (from 8.54 ppm to 8.87 ppm) and β-pyridyl protons H_b (from 7.68 ppm to 7.99 ppm) and both of them split into two set of signals (Fig. 2 *A* and *B*), in a similar fashion to what was observed in analogous reaction systems (43). ESI-TOF-MS provided further evidence for the stoichiometry of formation of **10**. Peaks at m/z = 877.3635, 1,220.1737, and 1,904.7172 were found (*SI Appendix*, Fig. S18), corresponding to $[\mathbf{10} - 4OTf]^{4+}$, $[\mathbf{10} - 3OTf]^{3+}$, and $[\mathbf{10} - 2OTf]^{2+}$, respectively.

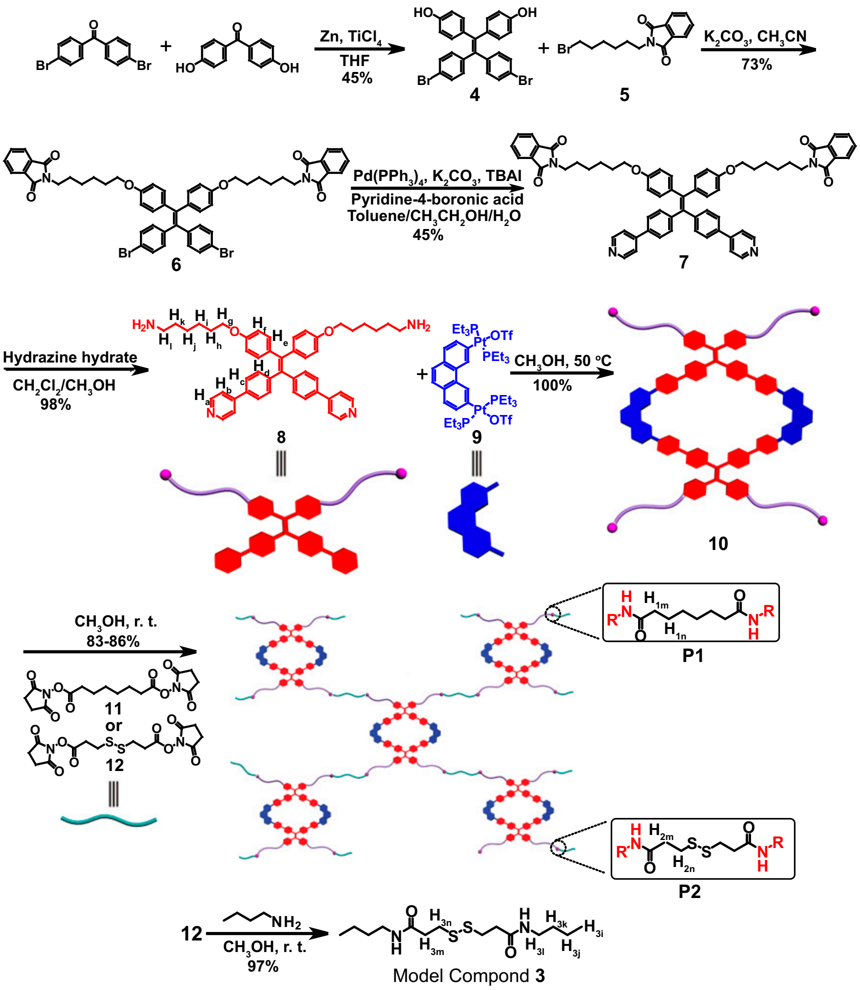

Fig. 1. Synthetic routes and cartoon representations of **P1** and **P2** and model compound **3**.

The $^{31}\text{P}\{^{1}\text{H}\}$ NMR spectra of **P1** and **P2** exhibit broader singlets but with chemical shifts similar to that of rhomboid **10** (Fig. 2 *G–I*), indicating that the metallacyclic structures were maintained in **P1** and **P2**. In the ^{1}H NMR spectra of **P1** and **P2**, the aminomethylene protons H_{l} shifted from 2.75 ppm to 3.18 ppm (Fig. 2 *B–D*) because the amidation reaction changes the chemical enviroment of H_{l}. No chemical shift changes were observed for the pyridyl protons H_{a}, H_{b} and the aromatic protons H_{c}, H_{d}, H_{e}, and H_{f}, indicating that the amidation reaction does not perturb the rhomboidal metallacycle **10**. To prove the efficiency of the amidation reaction, model compound **3** was also synthesized by stirring *n*-butylamine and linker **12** (2:1 molar ratio) overnight. Fig. 2*E* shows the ^{1}H NMR spectrum of the reaction mixture of **3** after 8 h. As seen, almost all of the reactants were consumed and a new peak for *N*-hydroxysuccinimide appeared, indicating the efficiency of the amidation reaction between alkylamine and *N*-hydroxysuccinimide-activated carboxylic acid. Moreover, protons H_{l}, H_{m}, and H_{n} of **P2** and compound **3** appear at the same location and all of them exhibit triplet signals, indicating that the amidation reaction was also highly efficient during the covalent linking process.

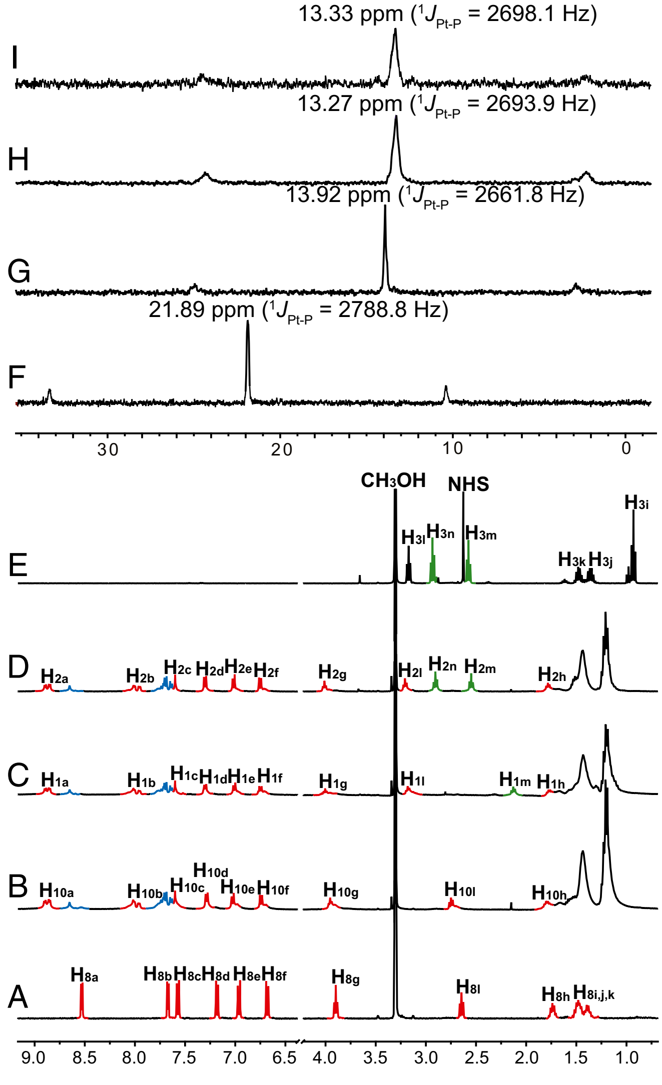

Fig. 2. NMR characterization ligand **8**, rhomboid **10**, **P1**, **P2**, and model compounds **3**. Partial (*A–E*) ^{1}H and (*F–I*) ^{31}P NMR spectra (CD_3OD, 295 K) of 120° ligand **8** (*A*), platinum acceptor **9** (*F*), rhomboid **10** (*B* and *G*), **P1** (*C* and *H*), **P2** (*D* and *I*) and reaction mixture of preparing model compound **3** (*E*). The peaks for protons of platinum acceptor **9** are marked in blue.

The morphology of **P1** and **P2** was characterized by scanning electron microscopy (SEM) (Fig. 3 and *SI Appendix*, Figs. S27–S32). The samples were prepared by dropping their methanol solution onto a silica wafer followed by evaporation. At lower concentrations (0.1 mg/mL), well-dispersed nanoparticles were observed (Fig. 3 *A* and *D*) for both **P1** and **P2**. However, when the concentration increased to 1.0 mg/mL, network structures emerged (Fig. 3 *B* and *E*) for both species, due to further aggregation of nanoparticles. We also found the coexistence of both dispersed nanoparticles and network structures at the edge of the silica wafer (*SI Appendix*, Figs. S29 and S32), which provides evidence for the concentration-dependent transformation of their morphology. The size of **P1** and **P2** was determined by dynamic light scattering (DLS). At a concentration of 0.1 mg/mL, **P1** and **P2** showed average hydrodynamic diameter (D_{h}) values of 296 and 283 nm (Fig. 3 *C* and *F*), respectively, consistent with the size of the particles observed by SEM (~250 to 310 nm).

The UV and visible (UV-Vis) absorption and fluorescence emission spectra of ligand **8**, rhomboid **10**, **P1**, and **P2** in methanol and methanol/water (1/9, vol/vol) are shown in Fig. 4. Ligand **8** displays two broad absorption bands centered at 262 and 336 nm with molar absorption coefficients (ε) of 3.30×10^{4} and 2.03×10^{4} $\text{M}^{-1}\cdot\text{cm}^{-1}$, respectively (Fig. 4*A* and *SI Appendix*, Table S1). Upon the formation of rhomboidal metallacycle **10**, the lowest energy band is moderately red-shifted (*ca*. 26 nm). Rhomboid **10** exhibits four absorption bands centered at 257, 266, 290, and 362 nm with $\varepsilon = 1.46 \times 10^{5}$, 1.48×10^{5}, 1.06×10^{5}, and 5.78×10^{4} $\text{M}^{-1}\cdot\text{cm}^{-1}$, respectively (Fig. 4*A* and *SI Appendix*, Table S1). The absorption spectra of **P1** and **P2** are quite similar to that of rhomboid **10**, providing further evidence for the retention of the rhomboidal metallacycle structures in **P1** and **P2**.

Ligand **8** is weakly emissive (Fig. 4*B*) in methanol because of the nonradiative decay via intramolecular rotations of the pyridyl and phenyl rings (7–11). Upon formation of rhomboid **10**, the pyridyl rings are partially rigidified, which limits their rotation, giving a moderate emission band centered at 522 nm. After the formation of **P1** and **P2**, the TPE derivatives further aggregate, making **P1** and **P2** even more emissive than their metallacycle precursor **10** (Fig. 4*B*). The absorption and emission spectra of the four species in methanol/water (1/9, vol/vol) are quite similar to that in methanol, except for the fluorescence intensity increases due to the AIE effects of TPE-type compounds in poor solvents (Fig. 4 *C* and *D*). The changes in quantum yields (Φ_{F}) in methanol and methanol/water (1/9, vol/vol) are in good agreement with the emission enhancement. In methanol, a very low Φ_{F} value (less than 0.05%) was observed for ligand **8**. For rhomboid **10**, the value rises to 0.237%. For **P1** and **P2**, the values further increase to 0.329 and 0.337%, respectively. While in methanol/water (1/9, vol/vol), the Φ_{F} value of ligand **8** increases to 1.22% due to the AIE effect. Correspondingly, the Φ_{F} values of rhomboid **10**, **P1**, and **P2** increase to 2.13, 2.77, and 2.89%, respectively (*SI Appendix*, Table S1).

The fluorescent properties of **P1** and **P2** inspired us to explore their applications as bioimaging agents. Confocal laser scanning microscopy (CLSM) was used to evaluate the cellular uptake efficiency and intracellular localization of **P2** in single cells. Based on the CLSM data, a bright fluorescence derived from **P2** was observed in the cytoplasm of the cells after 6 h of incubation (Fig. 5 *A–H*), suggesting that the polymers can be applied for cell imaging. Moreover, the emission spectrum of **P2** by CLSM (Fig. 5*I*) is consistent with their fluorescence spectra described above (Fig. 4 *B* and *D*), with maximum emission at 521 nm. This result suggests that the metallacycle structure remains intact during the imaging process. The fluorescence of **P1** and **P2** at different concentrations (40 and 200 μg/mL) was also collected by flow cytometric analysis (Fig. 5 *J* and *K*), indicating that **P1**

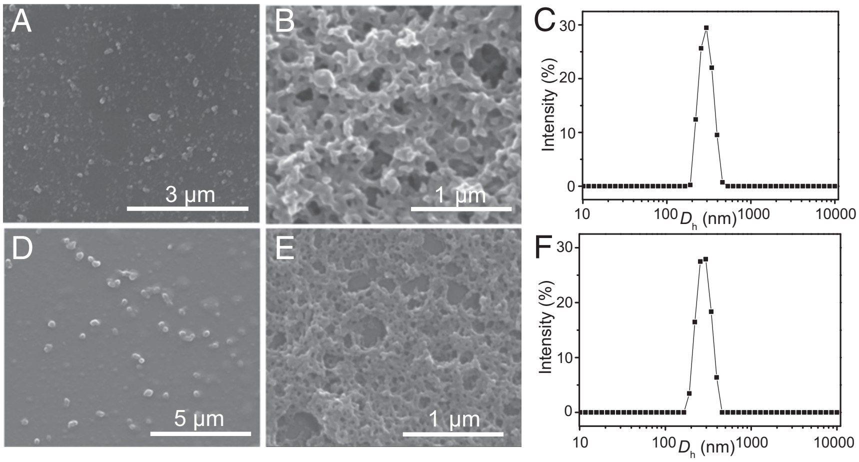

Fig. 3. Morphology and size analyses of **P1** and **P2**. (*A*) The formation of nanoparticles at the concentration of 0.1 mg/mL for **P1**. (*B*) The formation of network structures at the concentration of 1.0 mg/mL for **P1**. (*C*) Size distributions of **P1** in methanol at the concentration of 0.1 mg/mL. (*D*) The formation of nanoparticles at the concentration of 0.1 mg/mL for **P2**. (*E*) The formation of network structures at the concentration of 1.0 mg/mL for **P2**. (*F*) Size distributions of **P2** in methanol at the concentration of 0.1 mg/mL.

and **P2** serve as contrast agents for cell imaging in the concentration range of 40 μg/mL to 200 μg/mL.

In vivo experiments were performed to evaluate the efficiency and distribution of **P2** as contrast agent. Aqueous suspensions of **P2** at various concentrations (~7.8 to 500 μg/mL) were imaged using an in vitro phantom study. A linear dependence of the fluorescence intensity on concentration was observed in the tested range (Fig. 6*A*), revealing the potential of using **P2** for real-time imaging and quantitative analysis. To verify this, 20 μL of **P2** (10 mg/mL) was intratumorally injected into a mouse bearing an MDA-MB-231 (a human breast adenocarcinoma cell line) tumor. A significant fluorescence of the tumor was observed even 24 h after injection (Fig. 6*B*), indicating that **P2** is both chemostable and photostable in vivo, which is an essential criterion for bioimaging agents. The same mouse was killed 24 h after injection, and the tumor, major organs, and lymph nodes were imaged (Fig. 6*C*). A significant transfer of **P2** from the tumor to the liver and lung was observed. In addition, there was an accumulation of **P2** in lymph nodes, which is associated with tumor metastasis and early diagnostics. We next explored the in vivo distribution of **P2** in tumor-bearing mouse following systematic administration. By the investigation of the images and fluorescence counts of different organs 6 h after i.v. injection, we found that **P2** showed a significant enrichment in the lung over the other organs (Fig. 6 *D* and *E*). Hence, given the known anticancer activity of rhomboidal Pt(II) metallacycles (42), the possible use of these polymers toward lung cancer therapy could be explored.

Conclusion

In summary, by linking the rhomboidal metallacycles **10** via amidation reaction between *N*-hydroxysuccinimide-activated carboxylic acid and alkylamine, two polymers, **P1** and **P2**, were successfully prepared and characterized by multinuclear NMR (^{1}H and ^{31}P) and SEM. The structure of the metallacycles was maintained in the polymers due to the mild, highly efficient and catalysis-free amidation reaction, providing a method to polymerize metallacycles to give functional polymers and an alternative approach for postfunctionalization of metallacycles. The metal coordination limits the free rotation of the aromatic rings of TPE, and the formation and further aggregation of polymers match well with the AIE properties of TPE derivatives, thereby providing these polymers with enhanced fluorescence emission properties useful as bioimaging agents. Moreover, this covalent linking approach to aggregate AIE-type compounds also provides a good method to further enhance the AIE effects. The use of these fluorescent polymers as bioimaging agents was

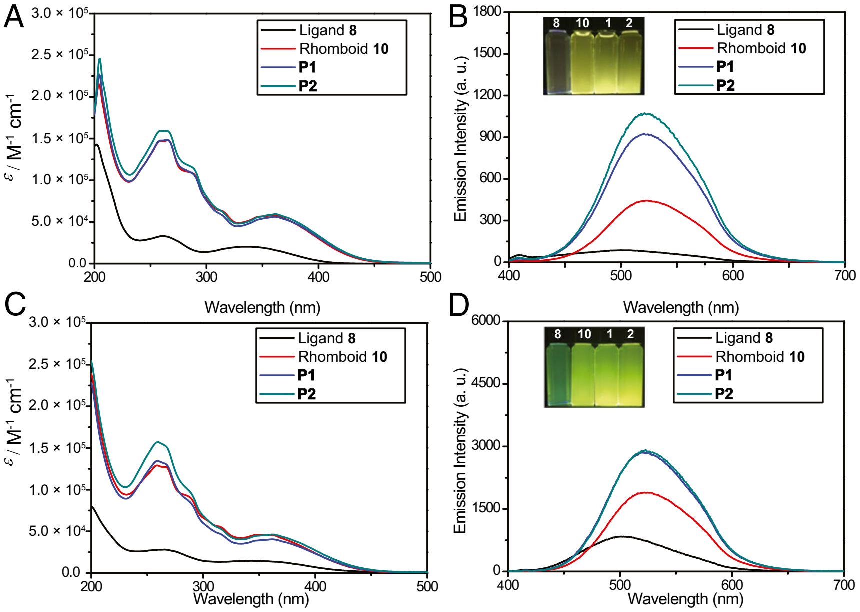

Fig. 4. Spectral characterization of ligand **8**, rhomboid **10**, **P1**, and **P2**. (*A*) UV-Vis absorption spectra of ligand **8**, rhomboid **10**, **P1**, and **P2** in methanol. (*B*) Fluorescence emission spectra of ligand **8**, rhomboid **10**, **P1**, and **P2** in methanol (λ_{ex} = 362 nm); (*Inset*) photograph of **8**, **10**, **P1**, and **P2** in methanol upon excitation at 365 nm using a UV lamp at 298 K. (*C*) UV-Vis absorption spectra of ligand **8**, rhomboid **10**, **P1**, and **P2** in 10%/90% methanol/water. (*D*) Fluorescence emission spectra of ligand **8**, rhomboid **10**, **P1**, and **P2** in 10%/90% methanol/water (λ_{ex} = 362 nm); (*Inset*) photograph of **8**, **10**, **P1**, and **P2** in 10%/90% methanol/water upon excitation at 365 nm using a UV lamp at 298 K. All of the concentrations are 10.0 μM; monomer concentration was used for **P1** and **P2**.

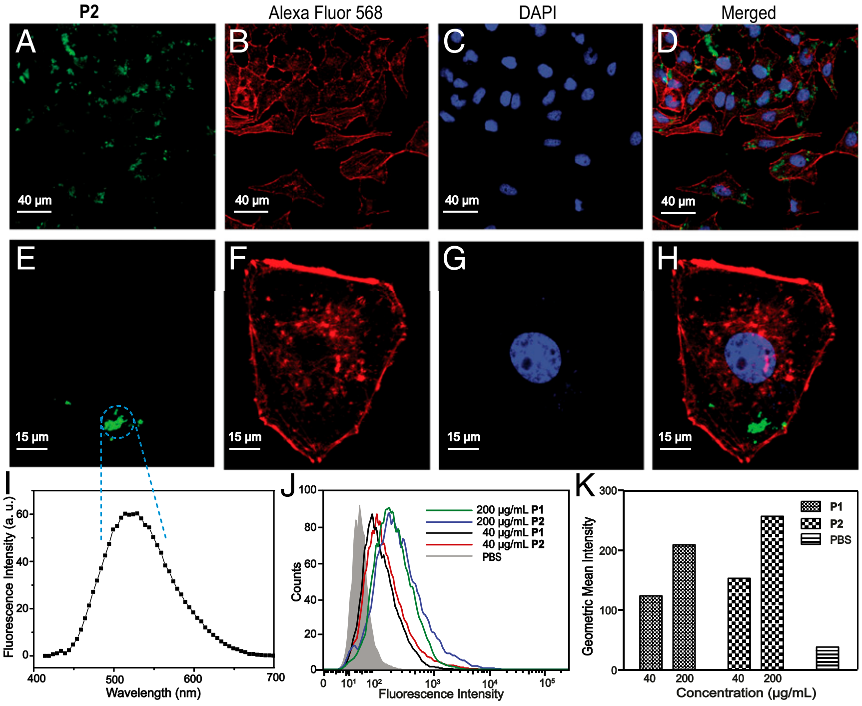

Fig. 5. CLSM images and flow cytometric analysis of A549R cells after incubation with **P1** and **P2**. (*A* and *E*) Images of cells treated with **P2**. (*B* and *F*) Images of cells stained with Alexa Fluor 568. (*C* and *G*) Images of cells stained with DAPI. (*D*) Merged image of A549R cells from *A*, *B*, and *C*. (*H*) Merged image of A549R cells from *E*, *F*, and *G*. (*I*) Fluorescence spectrum of **P2** in A549R cells taken by CLSM. (*J* and *K*) Flow cytometric analysis of **P1** and **P2** in A549R cells after 6 h of incubation.

explored, and their biodistribution after intratumoral and i.v. injection was also studied. A significant enrichment of the polymers in the lung was observed after i.v. injection. Other studies could explore further tuning the emission of the polymers by changing the linkers and the metallacycles, as well as their applications in bioimaging, drug delivery, and cancer therapy (42, 44–47).

Materials and Methods

All reagents were commercially available and used as supplied without further purification. Deuterated solvents were purchased from Cambridge Isotope Laboratory. Compounds **5** (48), **9** (49), **11** (39), and **12** (39) were prepared according to the literature procedures. NMR spectra were recorded on a Varian Unity 300-MHz or 400-MHz spectrometer. ^{1}H and ^{13}C NMR chemical shifts are reported relative to residual solvent signals, and ^{31}P{^{1}H}, NMR chemical shifts are referenced to an external unlocked sample of 85% H_3PO_4 (δ 0.0). Mass spectra were recorded on a Micromass Quattro II triple-quadrupole mass spectrometer using electrospray ionization with a MassLynx operating system. The melting points were collected on an SHPSIC WRS-2 automatic melting point apparatus. The UV-Vis experiments were conducted on a Hitachi U-4100 absorption spectrophotometer. The fluorescent experiments were conducted on a Hitachi F-7000 fluorescence spectrophotometer. Quantum yields were determined using quinine sulfate at 365 nm ($\Phi_F = 56\%$). SEM was performed on an FEI Quanta 600 FEG (field emission gun). CLSM was performed with a Zeiss LSM 710 Confocal Microscope using a 63× objective. Flow cytometry was performed with a Fluorescence Activated Cell Sorter Calibur Flow Cytometer (BD Biosciences). The size of polymers was measured using a Malvern ZS90 DLS instrument with an He–Ne laser (633 nm) and 90° collecting optics. The data were analyzed using Malvern Dispersion Technology Software 5.10. The mice were obtained from Beijing HFK Bioscience Co., Ltd.

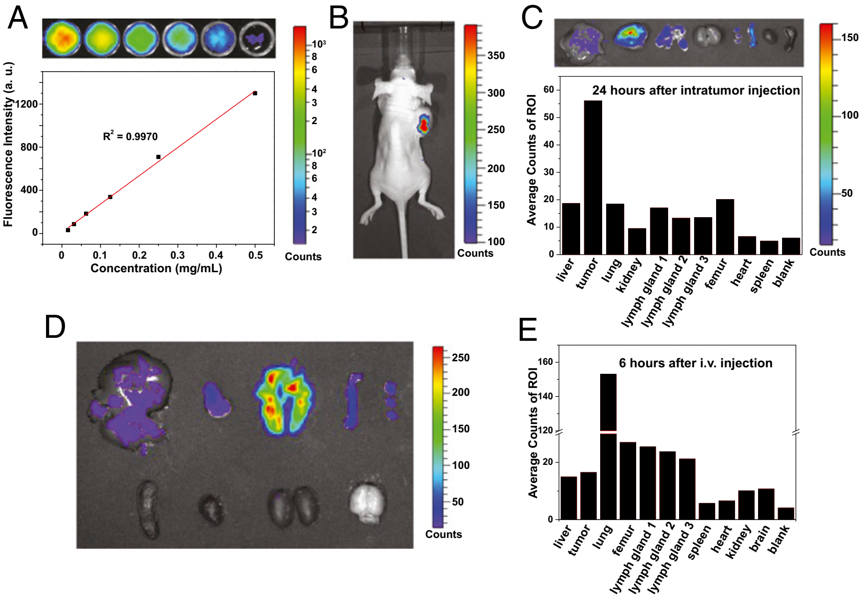

Fig. 6. Biodistribution and fluorescence images of **P2** in mice after intratumoral injection and i.v. injection. (*A*) Optical images of aqueous suspensions of different concentrations of **P2** in a 96-well plate, showing plot and fitting of the fluorescence intensity of **P2** versus their concentration. (*B*) Optical and fluorescence image of a mouse after intratumoral injection of 200 μg **P2**. The image was taken 24 h post injection. (*C*) Biodistribution of **P2** 24 h after intratumoral injection. The sequence of the images of the organs is the same as that of the fluorescence counts. (*D* and *E*) Optical and fluorescence images of a mouse after i.v. injection of 600 μg **P2**. (*D*) Images of different organs and (*E*) the fluorescence counts of different organs 6 h after i.v. injection. The sequence of the images of the organs is the same as that of the fluorescence counts. ROI, region of interest.

All animals received care in compliance with the guidelines outlined in the *Guide for the Care and Use of Laboratory Animals* (50). The procedures were approved by the University of Science and Technology of China Animal Care and Use Committee.

Rhomboid **10** was synthesized by heating **8** with **9** in a 1:1 molar ratio in a 2-dram vial. After cooling, the solvent was removed to give rhomboid **10** as a yellow solid. The formation of polymers **P1** and **P2** was achieved by stirring rhomboid **10** and linker **11** or **12** (1:2 molar ratio) in methanol (0.25 mmol/L for **10**) for 24 h. After that, the solvent was removed to give a crude product, which was dialyzed with methanol for another 24 h to give polymers that were then collected and dried under reduced pressure for future use.

Rhomboid **10**: ^{1}H NMR (400 MHz, CD_3OD, 295 K): 8.87 (m, 8H), 8.46–8.75 (m, 4H), 7.99 (m, 8H), 7.45–7.85 (m, 20H), 7.28 (d, $J = 8.2$ Hz, 8H), 7.02 (d, $J = 8.8$ Hz, 8H), 6.74 (d, $J = 8.8$ Hz, 8H), 3.95 (t, $J = 5.6$ Hz, 8H), 2.75 (t, $J = 7.0$ Hz, 4H), 0.90–1.90 (m, 152H). ^{31}P{^{1}H}, NMR (121.4 MHz, CD_3OD, 295 K) δ (ppm): 13.92 ppm (s, ^{195}Pt satellites, $^1J_{Pt-P} = 2{,}661.8$ Hz). ESI-TOF-MS: *m/z* 877.3635 ([**10** − 4OTf]$^{4+}$), *m/z* 1,220.1737 ([**10** − 3OTf]$^{3+}$), *m/z* 1,904.7172 ([**10** − 2OTf]$^{2+}$).

P1: ^{1}H NMR (400 MHz, CD_3OD, 295 K): 8.87 (m, 8H), 8.46–8.75 (m, 4H), 7.99 (m, 8H), 7.45–7.85 (m, 20H), 7.28 (d, $J = 8.2$ Hz, 8H), 7.02 (d, $J = 8.8$ Hz, 8H), 6.74 (d, $J = 8.8$ Hz, 8H), 4.00 (t, $J = 5.6$ Hz, 8H), 3.18 (t, $J = 7.0$ Hz, 8H), 2.13 (t, $J = 7.0$ Hz, 8H), 0.90–1.90 (m, 168H). ^{31}P{^{1}H} NMR (121.4 MHz, CD_3OD, 295 K) δ (ppm): 13.27 ppm (s, ^{195}Pt satellites, $^1J_{Pt-P} = 2{,}693.9$ Hz).

P2: ^{1}H NMR (400 MHz, CD_3OD, 295 K): ^{1}H NMR (400 MHz, CD_3OD, 295 K): 8.87 (m, 8H), 8.46–8.75 (m, 4H), 7.99 (m, 8H), 7.45–7.85 (m, 20H), 7.28 (d, $J = 8.2$ Hz, 8H), 7.02 (d, $J = 8.8$ Hz, 8H), 6.74 (d, $J = 8.8$ Hz, 8H), 4.01 (t, $J = 5.6$ Hz, 8H), 3.21 (t, $J = 7.0$ Hz, 8H), 2.91 (t, $J = 7.2$ Hz, 8H), 2.55 (t, $J = 7.2$ Hz, 8H), 1.78 (t, $J = 6.6$ Hz, 8H), 0.90–1.60 (m, 152H). ^{31}P{^{1}H} NMR (121.4 MHz, CD_3OD, 295 K) δ (ppm): 13.33 ppm (s, ^{195}Pt satellites, $^1J_{Pt-P} = 2{,}698.1$ Hz).

ACKNOWLEDGMENTS. P.J.S. acknowledges National Science Foundation Grant 1212799 for financial support. Y.-C.W. acknowledges National Natural Science Foundation of China Grants 51573176 and 51633008 for financial support.

1. Thomas SW, 3rd, Joly GD, Swager TM (2007) Chemical sensors based on amplifying fluorescent conjugated polymers. *Chem Rev* 107(4):1339–1386.
2. Basabe-Desmonts L, Reinhoudt DN, Crego-Calama M (2007) Design of fluorescent materials for chemical sensing. *Chem Soc Rev* 36(6):993–1017.
3. Kim HN, Guo Z, Zhu W, Yoon J, Tian H (2011) Recent progress on polymer-based fluorescent and colorimetric chemosensors. *Chem Soc Rev* 40(1):79–93.
4. Stuart MA, et al. (2010) Emerging applications of stimuli-responsive polymer materials. *Nat Mater* 9(2):101–113.
5. Yuan Y, Zhang C-J, Liu B (2015) A photoactivatable AIE polymer for light-controlled gene delivery: Concurrent endo/lysosomal escape and DNA unpacking. *Angew Chem Int Ed Engl* 54(39):11419–11423.
6. Shi B, et al. (2016) Nanoparticles with near-infrared emission enhanced by pillararene-based molecular recognition in water. *J Am Chem Soc* 138(1):80–83.
7. Mei J, Leung NL, Kwok RT, Lam JW, Tang BZ (2015) Aggregation-induced emission: Together we shine, united we soar! *Chem Rev* 115(21):11718–11940.
8. Luo J, et al. (2001) Aggregation-induced emission of 1-methyl-1,2,3,4,5-pentaphenylsilole. *Chem Commun (Camb)* (18):1740–1741.
9. Mei J, et al. (2014) Aggregation-induced emission: The whole is more brilliant than the parts. *Adv Mater* 26(31):5429–5479.
10. Zhao Z, Lam JWY, Tang BZ (2012) Tetraphenylethene: A versatile AIE building block for the construction of efficient luminescent materials for organic light-emitting diodes. *J Mater Chem* 22(45):23726–23740.
11. Hong Y, Lam JWY, Tang BZ (2011) Aggregation-induced emission. *Chem Soc Rev* 40(11):5361–5388.
12. Stang PJ, Olenyuk B (1997) Self-assembly, symmetry, and molecular architecture: Coordination as the motif in the rational design of supramolecular metallacyclic polygons and polyhedra. *Acc Chem Res* 30(12):502–518.
13. Leininger S, Olenyuk B, Stang PJ (2000) Self-assembly of discrete cyclic nanostructures mediated by transition metals. *Chem Rev* 100(3):853–908.
14. Fujita M, Tominaga M, Hori A, Therrien B (2005) Coordination assemblies from a Pd(II)-cornered square complex. *Acc Chem Res* 38(4):369–378.
15. Oliveri CG, Ulmann PA, Wiester MJ, Mirkin CA (2008) Heteroligated supramolecular coordination complexes formed via the halide-induced ligand rearrangement reaction. *Acc Chem Res* 41(12):1618–1629.
16. Northrop BH, Zheng Y-R, Chi K-W, Stang PJ (2009) Self-organization in coordination-driven self-assembly. *Acc Chem Res* 42(10):1554–1563.
17. De S, Mahata K, Schmittel M (2010) Metal-coordination-driven dynamic heteroleptic architectures. *Chem Soc Rev* 39(5):1555–1575.
18. Chakrabarty R, Mukherjee PS, Stang PJ (2011) Supramolecular coordination: Self-assembly of finite two- and three-dimensional ensembles. *Chem Rev* 111(11):6810–6918.
19. Cook TR, Zheng Y-R, Stang PJ (2013) Metal-organic frameworks and self-assembled supramolecular coordination complexes: Comparing and contrasting the design, synthesis, and functionality of metal-organic materials. *Chem Rev* 113(1):734–777.
20. Brown CJ, Toste FD, Bergman RG, Raymond KN (2015) Supramolecular catalysis in metal-ligand cluster hosts. *Chem Rev* 115(9):3012–3035.
21. Cook TR, Stang PJ (2015) Recent developments in the preparation and chemistry of metallacycles and metallacages via coordination. *Chem Rev* 115(15):7001–7045.
22. Newkome GR, Moorefield CN (2015) From 1 → 3 dendritic designs to fractal supramacromolecular constructs: Understanding the pathway to the Sierpiński gasket. *Chem Soc Rev* 44(12):3954–3967.
23. McConnell AJ, Wood CS, Neelakandan PP, Nitschke JR (2015) Stimuli-responsive metal-ligand assemblies. *Chem Rev* 115(15):7729–7793.
24. Lifschitz AM, Rosen MS, McGuirk CM, Mirkin CA (2015) Allosteric supramolecular coordination constructs. *J Am Chem Soc* 137(23):7252–7261.
25. Sautter A, et al. (2005) Ultrafast energy-electron transfer cascade in a multichromophoric light-harvesting molecular square. *J Am Chem Soc* 127(18):6719–6729.
26. Pollock JB, Schneider GL, Cook TR, Davies AS, Stang PJ (2013) Tunable visible light emission of self-assembled rhomboidal metallacycles. *J Am Chem Soc* 135(37):13676–13679.
27. Yan X, et al. (2014) Photoinduced transformations of stiff-stilbene-based discrete metallacycles to metallosupramolecular polymers. *Proc Natl Acad Sci USA* 111(24):8717–8722.
28. Chen LJ, et al. (2015) Hierarchical self-assembly of discrete organoplatinum(II) metallacycles with polysaccharide via electrostatic interactions and their application for heparin detection. *J Am Chem Soc* 137(36):11725–11735.
29. Fan J, Lal Saha M, Song B, Schönherr H, Schmittel M (2012) Preparation of a polynanocage dynamer: Correlating the growth of polymer strands using constitutional dynamic chemistry and heteroleptic aggregation. *J Am Chem Soc* 134(1):150–153.
30. Sun Q-F, Sato S, Fujita M (2012) An $M_{18}L_{24}$ stellated cuboctahedron through post-stellation of an $M_{12}L_{24}$ core. *Nat Chem* 4(4):330–333.
31. Yan X, Cook TR, Wang P, Huang F, Stang PJ (2015) Highly emissive platinum(II) metallacages. *Nat Chem* 7(4):342–348.
32. Kaphan DM, Levin MD, Bergman RG, Raymond KN, Toste FD (2015) A supramolecular microenvironment strategy for transition metal catalysis. *Science* 350(6265):1235–1238.
33. Yang H-B, et al. (2007) A highly efficient approach to the self-assembly of hexagonal cavity-cored tris[2]pseudorotaxanes from several components via multiple noncovalent interactions. *J Am Chem Soc* 129(46):14187–14189.
34. Li S, et al. (2013) Formation of [3]catenanes from 10 precursors via multicomponent coordination-driven self-assembly of metallarectangles. *J Am Chem Soc* 135(6):2084–2087.
35. Li S, et al. (2014) Self-assembly of triangular and hexagonal molecular necklaces. *J Am Chem Soc* 136(16):5908–5911.
36. Yan X, et al. (2013) Supramolecular polymers with tunable topologies via hierarchical coordination-driven self-assembly and hydrogen bonding interfaces. *Proc Natl Acad Sci USA* 110(39):15585–15590.
37. Yan X, et al. (2014) Responsive supramolecular polymer metallogel constructed by orthogonal coordination-driven self-assembly and host/guest interactions. *J Am Chem Soc* 136(12):4460–4463.
38. Li ZY, et al. (2014) Cross-linked supramolecular polymer gels constructed from discrete multi-pillar[5]arene metallacycles and their multiple stimuli-responsive behavior. *J Am Chem Soc* 136(24):8577–8589.
39. Kim E, et al. (2010) Facile, template-free synthesis of stimuli-responsive polymer nanocapsules for targeted drug delivery. *Angew Chem Int Ed Engl* 49(26):4405–4408.
40. Kim D, et al. (2010) Direct synthesis of polymer nanocapsules: Self-assembly of polymer hollow spheres through irreversible covalent bond formation. *J Am Chem Soc* 132(28):9908–9919.
41. Baek K, Hwang I, Roy I, Shetty D, Kim K (2015) Self-assembly of nanostructured materials through irreversible covalent bond formation. *Acc Chem Res* 48(8):2221–2229.
42. Grishagin IV, et al. (2014) In vivo anticancer activity of rhomboidal Pt(II) metallacycles. *Proc Natl Acad Sci USA* 111(52):18448–18453.
43. Yan X, et al. (2015) A suite of tetraphenylethylene-based discrete organoplatinum(II) metallacycles: Controllable structure and stoichiometry, aggregation-induced emission, and nitroaromatics sensing. *J Am Chem Soc* 137(48):15276–15286.
44. Cook TR, Vajpayee V, Lee MH, Stang PJ, Chi K-W (2013) Biomedical and biochemical applications of self-assembled metallacycles and metallacages. *Acc Chem Res* 46(11):2464–2474.
45. Zheng YR, Suntharalingam K, Johnstone TC, Lippard SJ (2015) Encapsulation of Pt(IV) prodrugs within a Pt(II) cage for drug delivery. *Chem Sci (Camb)* 6(2):1189–1193.
46. Zheng Y-R, et al. (2014) Pt(IV) prodrugs designed to bind non-covalently to human serum albumin for drug delivery. *J Am Chem Soc* 136(24):8790–8798.
47. Wilson JJ, Lippard SJ (2014) Synthetic methods for the preparation of platinum anticancer complexes. *Chem Rev* 114(8):4470–4495.
48. Kong X, et al. (2011) A mesogenic triphenylene-perylene-triphenylene triad. *Org Lett* 13(4):764–767.
49. Kryschenko YK, Seidel SR, Arif AM, Stang PJ (2003) Coordination-driven self-assembly of predesigned supramolecular triangles. *J Am Chem Soc* 125(17):5193–5198.
50. Committee on Care and Use of Laboratory Animals (1996) *Guide for the Care and Use of Laboratory Animals* (Natl Inst Health, Bethesda), DHHS Publ No (NIH) 85-23.